Independently Actuated Soft Magnetic Manipulators for Bimanual Operations in Confined Anatomical Cavities

Zaneta Koszowska, Michael Brockdorff, Tomas da Veiga, Giovanni Pittiglio, Peter Lloyd, Thomas Khan-White, Russell A. Harris, James W. Moor, James H. Chandler, and Pietro Valdastri*

Soft magnetic manipulators offer the prospect of improved surgical outcomes through their potential for miniaturization and inherently safe tissue interaction. However, independent actuation of multiple manipulators within the same confined workspace is limited by undesired simultaneous actuation and manipulator–manipulator interactions. Herein, for the first time, approaches for the independent magnetic actuation of two magnetic continuum manipulators within the same confined workspace are proposed. A novel modular magnetic soft robot segment design is proposed with modified geometry to provide preferential bending planes and high angles of deflection. This design is integrated into two dual-segment magnetic manipulators which, when arranged in parallel, can deliver independent bending in two planes of motion. Two distinct independent control strategies are proposed, based on orthogonal manipulator magnetization profiles and local field gradient control, respectively. Each dual-manipulator configuration is characterized over a sequence of applied magnetic fields and gradients, induced via a dual robotically controlled external permanent magnet system. Manipulator independence, bending range of motion, and twisting behaviors are evaluated as a function of control strategy and manipulator separation distance. To demonstrate the system's potential in clinical scenarios, a dual-manipulator configuration is adapted to carry an endoscopic camera and optic fiber, respectively. The resultant bimanual system is deployed in the confined anatomy of a skull-base phantom to simulate minimally invasive ablation of a pituitary adenoma. Independent motion of the camera and tool within the confined workspace demonstrate the potential for an independent magnetic tool manipulation for surgical applications.

1. Introduction

Modern surgical platforms such as the da Vinci (Intuitive Surgical da Vinci Surgical System, USA) and Versius (Cambridge Medical Robotics, UK) leverage robotic assistance for the precision control of multiple straight, rigid instruments.[1] This approach has delivered a step change in the provision of many minimally invasive procedures and has set a precedent for robotics in surgery. Driven by the aims of delivering improvements to anatomical conformation, achievable workspace, and surgical access requirements, numerous flexible continuum robotic devices have since been proposed.[2] Mechanically driven approaches have realized actuation via cables (Intuitive Surgical da Vinci Surgical System, USA), rods[3] or concentric tube interactions,[4] with complete robotic platforms having been proposed to deliver bimanual operations within confined anatomy.[5,6] Although sophisticated and effective approaches, integration of continuum tools based on mechanical assemblies of hard metallic structures imposes a reliance on the controller and/or operator to deliver safe (ideally contact free) tissue interaction

Z. Koszowska, M. Brockdorff, T. da Veiga, P. Lloyd, J. H. Chandler, P. Valdastri
Storm Lab UK
School of Electronic and Electrical Engineering
University of Leeds
Leeds LS2 9JT, UK
E-mail: p.valdastri@leeds.ac.uk

The ORCID identification number(s) for the author(s) of this article can be found under https://doi.org/10.1002/aisy.202300062.

G. Pittiglio
Department of Cardiovascular Surgery
Boston Children's Hospital
Harvard Medical School
Boston, MA 02115, USA

T. Khan-White
School of Medicine
Leeds Institute of Medical Research at St James's
Faculty of Medicine and Health
University of Leeds
Leeds LS9 7TF, UK

R. A. Harris
Future Manufacturing Processes Research Group
University of Leeds
Leeds LS2 9JT, UK

during deployment and use; something exacerbated within confined anatomy.

As an inherently safer alternative to mechanically driven designs, soft-bodied surgical robots have also been proposed.[7] Due to their high structural compliance (similar to that of soft tissues), interaction forces are limited, and passive anatomical conformation is possible. Soft robots intrinsically actuated via pneumatics[8,9] or hydraulics[10] have proven successful for endoscopic applications. However, due to the requirement for onboard actuation chambers and tubing connections, scaling designs down comes at the cost of reducing controllable degrees of freedom. Through the use of remote actuation, soft magnetic manipulators (SMMs) overcome this limitation, delivering virtually unlimited miniaturization potential without loss of controllable degrees of freedom.[11] SMMs maintain the advantages of a compliant structure and can be magnetically preprogrammed to produce desired deformations under the effect of controlled external magnetic fields.[12] These advantages have been demonstrated in a wide range of medical applications including cardiovascular,[13,14] bronchoscopic,[15] pancreatic,[16] and vasculature navigation.[17–19]

Driven by the requirements of precision, miniaturization, and delicate tissue interactions, SMMs represent a promising candidate for the evolution of robotic surgery in delicate confined anatomy. To date, SMMs have been investigated in single-manipulator set-ups mainly targeting endoluminal applications, precluding the delivery of multiple independent magnetic manipulators within a shared workspace. As endoscopic and laparoscopic procedures typically require multiple tools to be present at the operating site, systems providing solutions to independent SMM control would enable to expand the reach of magnetic approaches beyond endoluminal applications to bimanual surgical procedures. However, utilizing magnetic actuation strategies makes multitool set up challenging due to the complexity in achieving control independence over the magnetic agents. Considering two identical SMMs in a shared workspace, application of uniform magnetic field conditions would lead to the same motion for both agents.

Multiagent magnetic control was investigated at the microscale for control of untethered mobile micro-robots, swimmers, and spheres. Suggested approaches utilize geometric[20–24] or magnetic[25,26] heterogeneity between agents, as well as interagent magnetic interaction,[27,28] leading to different responses under application of a uniform magnetic field. Other approaches exploit sophisticated magnetic control such as systems of electromagnetic coils[29] of which some enable generation of nonuniform magnetic fields[30] or achieve independence in actuation of multiple magnetic degrees of freedom (DOFs).[31,32] All presented research in the area of independent magnetic control has investigated untethered robots at micro-scale actuated in a fluid medium. The issue of independent control of continuum SMMs within a confined workspace still remains an open challenge.

In the presented work, we investigate for the first time the concept of parallel bimanual SMMs under independent magnetic control within a shared confined workspace, as depicted in **Figure 1**. We develop a modular monolithic double-helix SMM design that promotes bending within a desired plane through mechanical constraint. Manipulator designs capable of biplane bending are developed through serial stacking of the modular SMM design and are arranged into parallel dual-manipulator configurations with separations between 2 and 4 cm. To deliver independent control, we present and compare two distinct approaches, based on orthogonal SMM magnetization profiles and local field gradient control, respectively. Each dual-manipulator configuration is characterized in terms of independent bending and twisting behaviors under applications of magnetic fields and field gradients, as generated using our dual robotically controlled external permanent magnet system (dEPM).[33] Interaction forces between manipulators and their effect on desired poses are considered for a range of workspace configurations, and we determine the minimum operational workspace possible for bimanual operation using the presented manipulators.

To demonstrate our bimanual SMM system within a clinically relevant scenario, we consider the case of endoscopic endonasal transsphenoidal (EET) procedures for surgical treatment of pituitary tumors (which account for up to 15% of all intracranial masses and exhibit an estimated prevalence of 17% within the general population[34]). EET procedures currently involve insertion of a slender rigid endoscope and surgical tools through the nostrils to access the base of the brain. Although offering advantages over access via craniotomy, risks of nasal septal perforation, impaired olfactory function, and damage to nearby nerves and large blood vessels remain.[35] Many of these adverse outcomes are the result of manipulating multiple rigid instruments within the narrow, curved anatomy of the nasal cavity, and thus may be mitigated through the use of soft, compliant tools. Through configuration of our dual manipulators to carry an endoscopic camera and optic fiber, respectively, we present a concept of bimanual multitool magnetically actuated robotic system for minimally invasive ablation of a pituitary adenoma. We present independent motion of the camera and optic fiber within an anatomically accurate skull base phantom with simulated tumor, demonstrating for the first time the potential for independent magnetic tool manipulation within confined anatomy.

2. Results

Neglecting interaction forces between multiple SMMs, designs with equal magnetization profiles and controlled within a shared homogeneous magnetic field, will produce identical actuation outcomes. Independent control is possible through deployment of sophisticated magnetic field actuation (fields and gradients) and/or via optimization of the geometric or material properties of each SMM. The following considers the magnetic actuation principles involved in manipulator control to develop a modular geometric SMM segment design approach that promotes uniplanar bending. A multisegment integration is subsequently presented based on this design and coupled with magnetic field and gradient control strategies, enabled via the dEPM system, to promote independent control for application suitability.

J. W. Moor
ENT Department
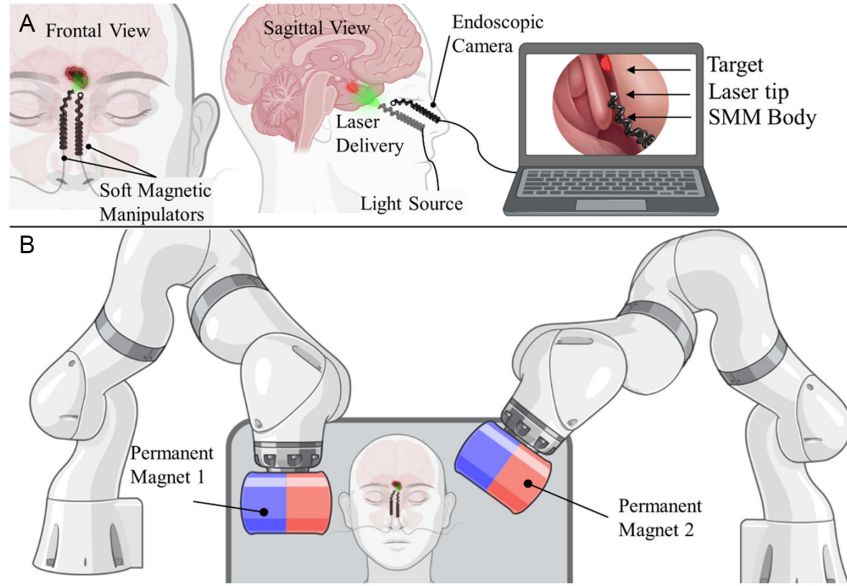Leeds Teaching Hospitals NHS Trust
Leeds LS1 3EX, UK

Figure 1. Overview of a magnetically actuated dual-manipulator set up. A) Actuated camera view – visible workspace and manipulator equipped with a fiber. B) Proposed set up in an operating room, permanent magnets mounted on robotic arms for controlled field generation.

2.1. Principle of Magnetic Actuation

A magnetic element with magnetization μ is subject to magnetic force f and torque τ, under an applied field B, respectively, as

$$f(p) = \nabla(\mu \cdot B(p)) \tag{1}$$

$$\tau(p) = \mu \times B(p) \tag{2}$$

At position $p \in R^3$ in space, where p is referred to as the focal point, or the point in the workspace where we aim to control a specific field and gradient. Lower case bold letters represent vectors (e.g., $v = [v_x v_y v_z]^T$), and the gradient operator ∇ represents partial derivatives in each of the three basis directions in the form $\nabla = [\frac{\partial}{\partial x} \frac{\partial}{\partial y} \frac{\partial}{\partial z}]^T$. Magnetic gradients allow for the generation of force, while magnetic field misalignments generate torques on a magnetic element. Considering a workspace with $x, y,$ and z axes, Equation (1) and (2) could be further expanded as

$$f(p) = \begin{bmatrix} f_x \\ f_y \\ f_z \end{bmatrix} = \begin{bmatrix} \mu_x & \mu_y \mu_z & 0 & 0 \\ 0 & \mu_x & 0 & \mu_y & \mu_z \\ -\mu_z & 0 & \mu_x & -\mu_z & \mu_y \end{bmatrix} \begin{bmatrix} \frac{\partial B_x(p)}{\partial x} \\ \frac{\partial B_x(p)}{\partial y} \\ \frac{\partial B_x(p)}{\partial z} \\ \frac{\partial B_y(p)}{\partial y} \\ \frac{\partial B_y(p)}{\partial z} \end{bmatrix} \tag{3}$$

$$\tau(p) = \begin{bmatrix} \tau_x \\ \tau_y \\ \tau_z \end{bmatrix} = \begin{bmatrix} 0 & -\mu_z & \mu_y \\ \mu_z & 0 & -\mu_x \\ -\mu_y & \mu_x & 0 \end{bmatrix} \begin{bmatrix} B_x(p) \\ B_y(p) \\ B_z(p) \end{bmatrix} \tag{4}$$

Magnetic actuation through the use of two external permanent magnets, such as the dEPM platform,[33] allows for individual control of magnetically induced forces and torques on magnetic objects. Pittiglio et al.[33] showed how the dEPM platform could

be used to independently control the wrench of a magnetic object. This was done by using homogenous fields to control the torque and linear gradients to control the forces. In this study, we propose an alternative method to generate magnetic torques in addition to using homogenous fields.

Consider that the general field at point p can be expressed as

$$B(p) = B(p_o) + \frac{\partial B(p)}{\partial p}(p - p_o) \tag{5}$$

where p_o is a position at a distance $\gamma \in \mathbb{R}^3$ away from p. This is the center of the gradient, where the field changes its polarity. When $p = p_o$ and applying only linear gradients, the field at position p is equal to 0. When $p \neq p_o$, a magnetic gradient is centered p_o, while the object we aim to control is at the focal point p. Therefore, at p, both magnetic field and gradient will be present. This equation is valid under the assumption that the gradient is constant over the workspace, that the divergence and curl of the magnetic field are zero, and that we are operating in a current-free workspace.

Under these magnetic conditions, a magnetic agent, such as an SMM with appropriate mechanical and magnetic design, could be manufactured to only exhibit torque when presented with certain combinations of magnetic fields and gradients simultaneously.

2.2. Segment Design

To balance the requirements for miniaturization, tool integration, and high bending-to-torsional stiffness, a monolithic (single material) design consisting of a soft magnetic double helix wrapped around a soft magnetic core is proposed, **Figure 2**. The design aims to deliver variation in bending stiffness between the two bending planes (XZ and YZ), as depicted in Figure 2. The
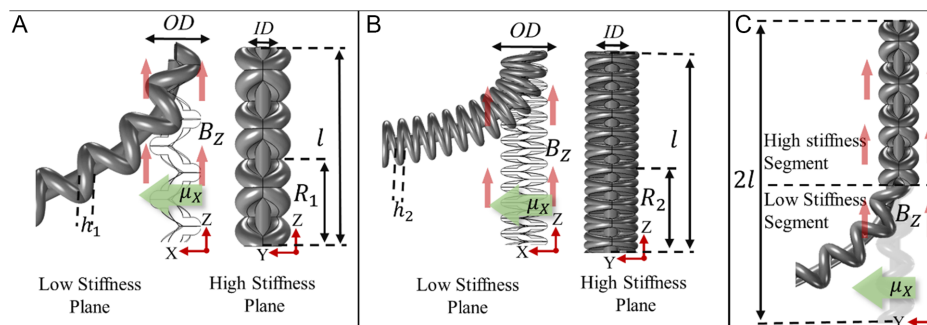
ADVANCED
SCIENCE NEWS

www.advancedsciencenews.com

ADVANCED
INTELLIGENT
SYSTEMS

www.advintellsyst.com

Figure 2. Examples of monolithic reinforcement designs, where h is the thickness of the helical structure, R is the number of revolutions per unit length, OD is the outer diameter and ID the inner diameter, l is the segment length, μ is the magnetization direction and Bz applied field direction. A) Represents two orthogonal projections of design low density SMM, showcasing characteristic variety of the manipulator between YZ and XZ planes. B) Represents high density SMM. C) An example of a two-segment manipulator using a low-density SMM design.

seam of the double helix intersecting points creates planar reinforcement, leading to significantly increased bending stiffness along the XZ plane. Constraining the motion of the SMM in this way allows for separation of actuation planes for segments arranged orthogonally in series (Figure 2C), as required for independent control.

We explore two different designs of the double helix structure, investigating its effect on the stiffness in XZ and YZ planes of the manipulator. The helical thickness (h) and the number of helical revolutions per unit length (R) are chosen as variables in this study. The increase in R (symmetrically for left and right-handed helix) adds more intersecting points along the length, therefore increases stiffness along the XZ plane. The decrease in helical thickness, however, is expected to promote bending in YZ plane. Therefore, in this study, we consider two designs with different h values, where both designs are characterized with maximum R (where further increase of this parameter would not create a double helix structure but a cylinder). Both designs are fabricated with outer diameter of 3.5 mm, considering endonasal application, and inner diameter of 1 mm for incorporating an internal tool channel for further instrumentation of the manipulator.

Two single-segment candidate SMM designs were evaluated in terms of their bending and twisting capacity in comparison to a baseline cylindrical SMM, in accordance with parameters presented in **Table 1**.

2.2.1. Segment Fabrication

Candidate helical designs and a cylinder (Table 1) were fabricated by casting with 3D-printed molds (Grey V4 resin, Form III, Formlabs, USA). Silicone (Dragon Skin 10, Smooth-On, Inc., U.S.A.) was mixed with 100 wt% (percentage by weight) of hard magnetic microparticles (Nd-FeB with an average 5 μm diameter,

MQFP-B+, Magnequench GmnH, Germany). The magnetic slurry was then mixed in a high vacuum mixer (ARV-310, THINKYMIXER, Japan) for 90 s at a speed of 1400 rpm and a pressure of 20.0 kPa. The degassed slurry was injected into closed molds and cured at 45 °C for 30 min.

Each design was fabricated twice to be magnetized in two directions for testing: along their X and Y axes, respectively, allowing for comparison of stiffness variability between the axes. The monolithic approach is fully soft and can be miniaturized further for access to the narrowest anatomical features.

2.2.2. Segment Design Evaluation

To understand the mechanical stability of the designs and the maximum expected bending under varying field conditions, fabricated designs magnetized in X and Y axes (Figure 2) were evaluated by recording manipulator deformation under application of homogenous magnetic field conditions as detailed in **Table 2**.

To generate homogeneous magnetic fields, the robotic arms of the dEPM system (**Figure 3**) positioned two external permanent magnets (101.6 mm × 101.6 mm) symmetrically with respect to each other and the sample's workspace. The experimental set up also included four Optitrack (OptiTrack, NaturalPoint, Inc., USA) infra-red cameras for 3D motion tracking and for calibration of magnets in space. The tip poses of manipulators were recorded via the optical tracking system through optical markers attached to the manipulator during testing. Bending angles around X, Y (γ_x and γ_y, respectively) and the torsional rotation angle around Z (γ_z) were computed from the rigid body rotations of the marker frame (0.33 g). Since we aim at minimizing torsion (γ_z) with respect to bending (γ_x and γ_y), we consider ratio

$$\rho_x = \frac{\gamma_x}{max\gamma_z}; \quad \rho_y = \frac{\gamma_y}{max\gamma_z} \quad (6)$$

Table 1. Design parameters for tested designs of magnetic manipulators.

Design	OD [mm]	ID [mm]	L [mm]	R	h [mm]	w [mm]
Cylinder	3.5	N/A	20	N/A	N/A	N/A
Low-Density SMM	3.5	1	20	5.5	1.5	1.25
High-Density SMM	3.5	1	20	16	0.5	1.25

Table 2. Magnetic field conditions in time applied during testing of three candidate designs in dEPM platform.

Time	0–20 s	20–40 s	40–60 s	60–80 s	80–100 s	100–120 s
Field Direction [10 mT]	X	−X	Z	−Z	Y	−Y

**ADVANCED
SCIENCE NEWS**
www.advancedsciencenews.com

**ADVANCED
INTELLIGENT
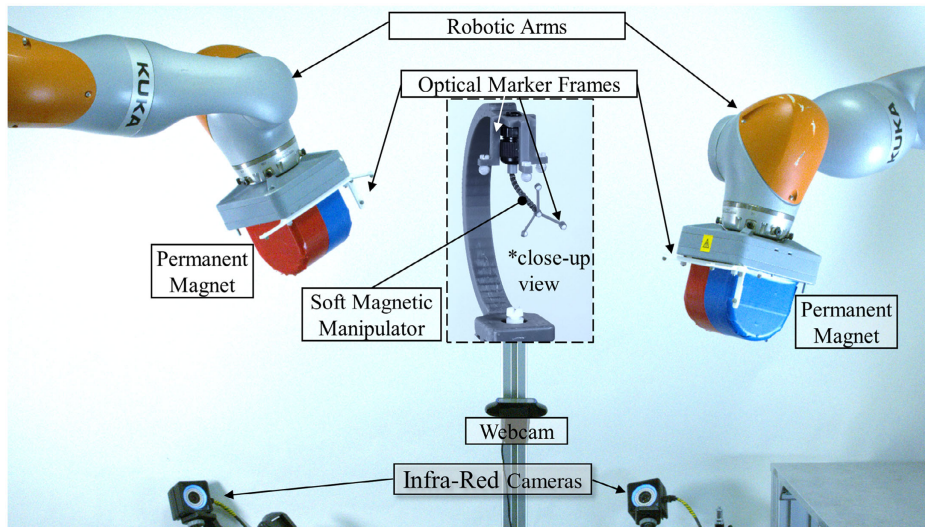SYSTEMS**
www.advintellsyst.com

Figure 3. Experimental set-up including dual external permanent magnet (dEPM) platform, infra-red cameras and soft magnetic manipulator (SMM) with optical marker frame at the base and tip.
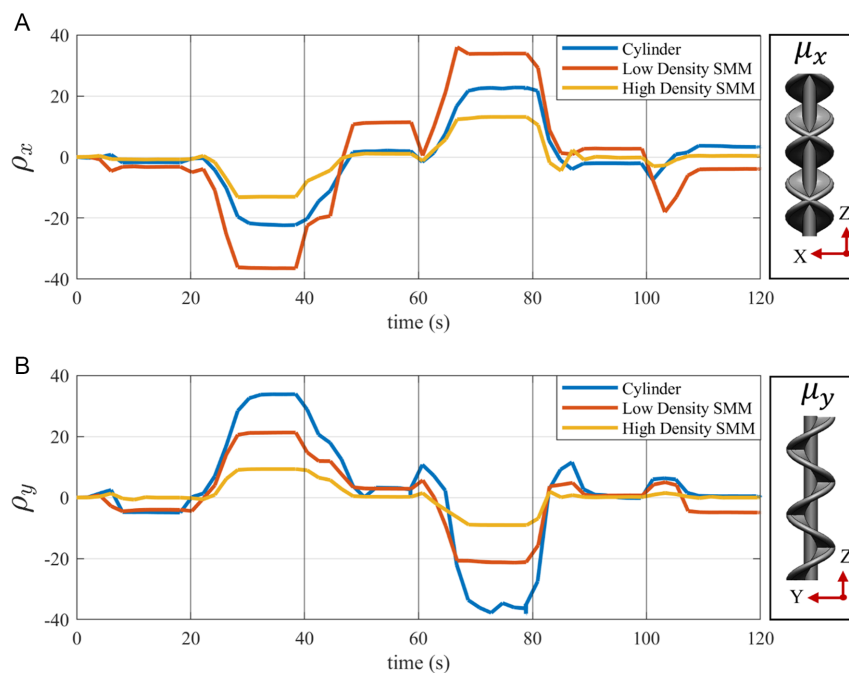

Figure 4. Results of testing three candidate designs under varied magnetic field conditions as a ratio of deflection to torsion. A) Ratio of deflection about Y axis to torsion for SMMs magnetized in X direction. B) Ratio of deflection about X axis to torsion for samples magnetized in Y direction.

where ρ_x corresponds to the low stiffness axis (**Figure 4**A) and ρ_y to the high stiffness axis (Figure 4B). For an ideal design, the ratio ρ_y would be lower than ρ_x as this implies a desired difference in bending response between XZ and YZ planes.

Analyzing bending behavior in both directions is motivated by the objective of maximizing the bending angle of a manipulator on one plane, while providing stability on the other.

In Figure 4A, low-density SMM shows a greater ratio ρ_x than a cylinder of the same diameter. In addition, in Figure 4A, the

ratio ρ_x value for high-density SMM is lower than the value for both cylinder and low-density SMM. In Figure 4B, cylindrical SMM shows the highest ratio ρ_y of all three samples. However, when analyzing both plots, only the low-density SMM shows the desired behavior in both magnetization cases. In the case of magnetization along X axis, the optimal design is expected to have the high ratio ρ_x and relatively low ratio ρ_y.

Collected results confirm that both structurally modified designs experience higher bending angle in YZ under a

2300062 (5 of 16)

ADVANCED
SCIENCE NEWS
www.advancedsciencenews.com

ADVANCED
INTELLIGENT
SYSTEMS
Open Access
www.advintellsyst.com

directionally varied 10 mT field, with respect to a cylinder. The *XZ* plane in the design concept is constrained by overlapping helices, creating a planar reinforcement. This provides increased stiffness in that plane, leading to reduced bending under the same actuating field, in comparison to *YZ* plane. Therefore, the bending performance of designs with a double helix feature is better than that of a typical cylindrical SMM.

Based on the analysis of experimental data, the low-density SMM presents the most suitable candidate for the objective of maximized bending in *YZ* plane and increased stiffness in *XZ* plane and was thus utilized for integration into more complex multisegment designs.

2.3. Modular Design for Independent Control

The double helix SMM segment design promotes bending motion of the manipulator in one axis. Combining segments in series and in orthogonal direction allows for enhanced separation of bending primitives under independent segment actuation (Figure 2C and 5C).

To realize independent actuation of multiple segments in the same workspace, specific combinations of magnetization profiles and actuating fields are required. As depicted in Figure 5, we propose to achieve this using a modular design with two manipulators in parallel (four SMM segments in total). Two strategies for independent control of the two manipulators within the same confined workspace are proposed, as depicted in **Figure 6** and **7**, respectively. The first, orthogonal magnetization (OM) strategy (Figure 6), utilizes segments with both axial and nonaxial magnetic moments in conjunction with either applied homogenous fields or linear field gradients. This is based on Pittiglio et al.,[33] where it is shown that when considering multiple magnetic objects, each having their own magnetization μ, maximum independent DOF control is achieved when the dipole direction of the two magnetic agents is orthogonal.

The second is referred to as parallel magnetization (PM) strategy (Figure 7) and employs axially magnetized segments in conjunction with magnetic gradients only, as detailed below.

2.3.1. Orthogonal Magnetization Strategy

In the OM strategy, the left manipulator base and tip segments, SMM_{LB} and SMM_{LT} respectively, are magnetized along the *z*-axis ($\mu_{\text{SMM}_{LB}} = \mu_{\text{SMM}_{LT}} = \mu_z$), while for the right manipulator the base and tip segments, SMM_{RB} and SMM_{RT}, respectively, are magnetized along the *x*-axis ($\mu_{\text{SMM}_{RB}} = \mu_{\text{SMM}_{RT}} = \mu_x$), see Figure 6A. The required magnetic fields and gradients for independent control of each manipulator were determined based on Equation (4), and reported in **Table 3**. Figure 6B showcases bending modalities of segments and required wrenches for each motion. Analysis of
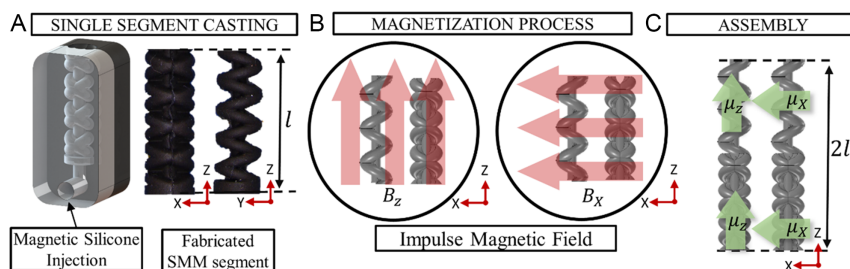

Figure 5. Fabrication process of SMMs. A) Single segment casting. B) Magnetization process of segments along their *Z* and *X* axes. C) An example of magnetized and assembled dual-segment manipulators.
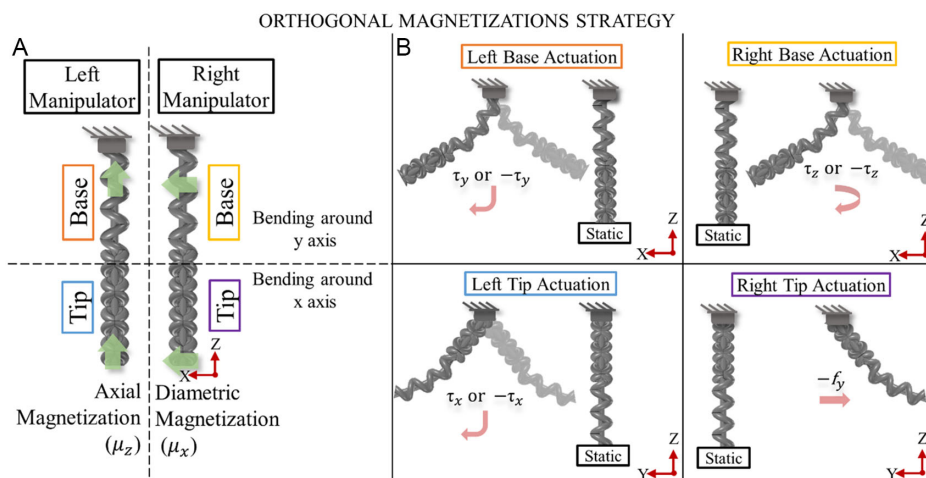

Figure 6. A case of two manipulators magnetized orthogonally; A) left manipulator (base and tip) magnetized along its main axis (*Z*). Right manipulator (base and tip) magnetized along its *X* axis. B) Representation of available DOFs in this configuration and wrenches needed to actuate each segment.

**ADVANCED
SCIENCE NEWS**

www.advancedsciencenews.com

**ADVANCED
INTELLIGENT
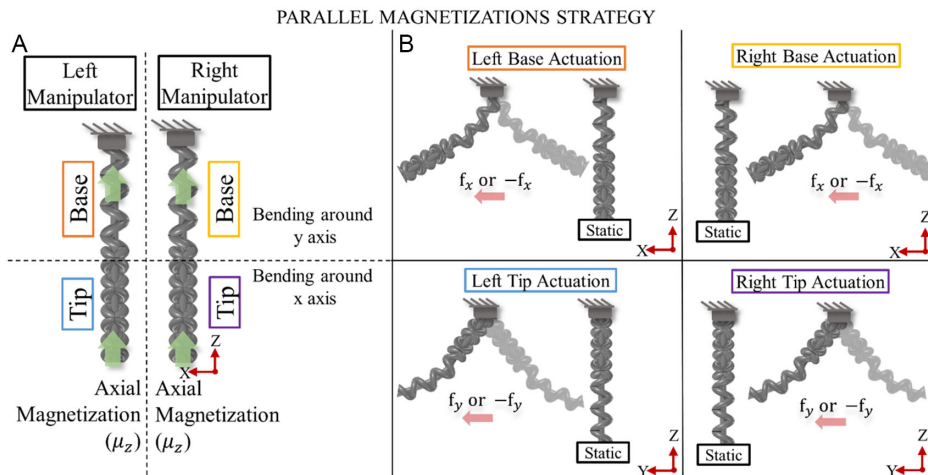SYSTEMS**
Open Access

www.advintellsyst.com

Figure 7. A case of two manipulators magnetized axially; A) Left and right manipulators (base and tip) magnetized along its main axis Z. B) Representation of available DOFs in this configuration and wrenches needed to actuate each segment.

Table 3. Wrench applied on agents 1 and 2 under applied field and gradients and their bending response in orthogonal magnetization case.

		Wrench applied on agent		Direction of bending	
		Left manipulator	Right manipulator	Left manipulator	Right manipulator
Fields and gradients	B_x	τ_y	0	$+x$ axis	None
	$-B_x$	$-\tau_y$	0	$-x$ axis	None
	B_y	$-\tau_x$	τ_z	$-y$ axis	τ_z
	$-B_y$	τ_x	$-\tau_z$	$+y$ axis	$-\tau_z$
	B_z	0	$-\tau_y$	None	$-x$ axis
	$-B_z$	0	τ_y	None	$+x$ axis
	$\frac{\partial B_z}{\partial y}$	0	f_y	None	$+y$ axis
	$-\frac{\partial B_z}{\partial y}$	0	$-f_y$	None	$-y$ axis

Table 3 shows that while moving the left manipulator along the y-axis, an undesired rotation of the right manipulator around the Z axis occurs. Further analysis of this phenomenon is discussed in Section 2.3.3.

2.3.2. Parallel Magnetization Strategy

Another method to independently control two SMMs could be achieved by using the actuation method proposed previously in Section 2.1. In this scenario, a magnetic gradient is applied at position p_o. The magnetic actuation at position p will be equal to the magnetic gradient applied at p_o as well as an induced magnetic field as described by Equation (5). This method allows for independent control between two manipulators, by setting p_o to the position of the static SMM (depicted as "static" in Figure 7B) and p to the position of the SMM that is meant to be actuated in a given case.

Unlike when using homogenous fields to control the torque, with this method we can achieve independent control of the SMMs regardless of the magnetization profile of the "static" SMM. This is because keeping the SMM stationary relies on having no field present at the position of the stationary SMM. This is in contrast to using homogenous fields, where in order for the SMM not to exhibit any torque, its magnetization must be aligned with applied magnetic field direction.

To evaluate this strategy, two SMMs were magnetized along Z axis ($\mu_{SMM_{LB}} = \mu_{SMM_{LT}} = \mu_{SMM_{RB}} = \mu_{SMM_{RT}} = \mu_z$), see Figure 7A. The distance γ is set to the distance between the two SMMs, such that $\gamma = [0 \quad D \quad 0]^T$. **Table 4** shows the magnetic field and gradient applied to independently control the two SMMs, along with the focal point selected.

It is evident that when controlling either manipulator to bend along the Y axis, the applied gradient also causes a force along Z axis on both manipulators. However, this force is much smaller than the desired torque and thus may be considered to have negligible influence on the resultant manipulator motion. The resultant direction of bending for the proposed applied field gradients is summarized in Table 4.

2.3.3. Independent Control Characterization

The motion independence of the parallel multisegment designs (Figure 6 and 7) was initially evaluated through testing with the dEPM platform. As well as motion independence, the tests also evaluated the maximum achievable range of motion and the smallest possible distance between the two manipulators before magnetic self-attraction causes adherence, an inherent risk with mechanically independent magnetized elements. The testing protocol was repeated for the OM and PM strategies to allow direct comparison between the two.

For each experiment, the two manipulators under test were positioned within the magnetic workspace with a separation distance D, in mechanical configurations as shown in **Figure 8**. An optical tracking system (OptiTrack, NaturalPoint, USA) was used to track the tip position and orientation of both manipulators at all times. The frames with optical markers weigh 0.27 and 0.17 g for left and right manipulators, respectively. For the OM

Table 4. Wrench applied on left and right manipulators under applied gradients and their bending response with the parallel magnetization strategy.

|		Focal point	Wrench applied on agent		Direction of bending	
			Left manipulator	Right manipulator	Left manipulator	Right manipulator
Fields and gradients	$\frac{\partial B_x}{\partial y}$	p_2	τ_y	0	$+x$ axis	None
	$-\frac{\partial B_x}{\partial y}$	p_2	$-\tau_y$	0	$-x$ axis	None
	$\frac{\partial B_y}{\partial y}$	p_2	$-f_z - \tau_x$	$-f_z$	$-y$ axis and pulled downward	Pulled downward
	$-\frac{\partial B_y}{\partial y}$	p_2	$f_z + \tau_x$	f_z	$+y$ axis and pushed upward	Pushed upward
	$\frac{\partial B_x}{\partial y}$	p_1	0	τ_y	None	$+x$ axis
	$-\frac{\partial B_x}{\partial y}$	p_1	0	$\tau-y$	None	$-x$ axis
	$\frac{\partial B_y}{\partial y}$	p_1	$-f_z$	$-f_z - \tau_x$	Pulled downward	$-y$ axis and pulled downward
	$-\frac{\partial B_y}{\partial y}$	p_1	f_z	$f_z + \tau_x$	Pushed upward	$+y$ axis and pushed upward
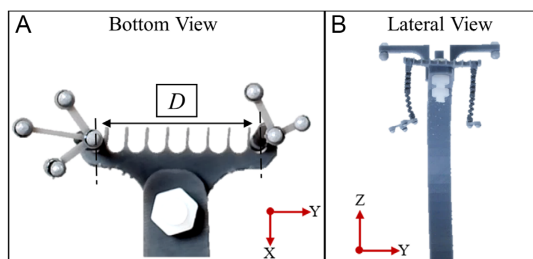
Figure 8. Experimental set-up. A) Bottom view of SMMs with optical marker frames at their tips, with highlighted D. B) Lateral view.

manipulators, magnetic fields identified in **Table 5** were applied in sequence to actuate segments SMM$_{LB}$, SMM$_{LT}$, SMM$_{RB}$, SMM$_{RT}$ consecutively. This actuation process was repeated for decreasing separation distances D ranging from 4 cm to 2 cm in steps of 0.5 cm. This testing process was repeated for the PM manipulators through sequential application of the field gradients identified in **Table 6**.

The tracked tip positions for the two manipulators during sequential field and/or gradient application for the OM and PM strategies are shown in **Figure 9** and **10**, respectively. The data illustrate that a level of independent motion is achievable using the two control strategies at a range of separation distances. Undesired manipulator motions (those recorded on the unactuated manipulator) are also present and show dependence on

Table 5. Conditions of magnetic fields, their direction, and magnitude applied in experiments for orthogonal magnetization strategy.

	Direction of bending	Magnetic field conditions [mT and mT m^{-1}]
Left manipulator	$-x$; x	$Bx = [-3; -4; -5; -6; -7; 3; 4; 5; 6; 7]$
	$-y$; y	$By = [-3; -4; -5; -6; -7; 3; 4; 5; 6; 7]$
Right manipulator	$-x$; x	$Bz = [-3; -4; -5; -6; -7; 3; 4; 5; 6; 7]$
	$-y$	$dBx/dy = [-50; -75; -100; -125; -150]$
	y	$dBx/dy = [50; 75; 100; 125; 150]$

Table 6. Conditions of magnetic field gradients, their direction, and magnitude applied in experiments for parallel magnetization strategy.

	Direction of bending	Magnetic field conditions [mT m^{-1}]
Left manipulator	$-x$, x	$dBx/y = [-50; -75; -100; -125; -150; 50; 75; 100; 125; 150]$
	$-y$; y	$dBy/y = [-50; -75; -100; -125; -150; 50; 75; 100; 125; 150]$
Right Manipulator	$-x$, x	$dBx/y = [-50; -75; -100; -125; -150; 50; 75; 100; 125; 150]$
	$-y$, y	$dBy/y = [-50; -75; -100; -125; -150; 50; 75; 100; 125; 150]$

control strategy, actuated DOF, and separation distance. These motions are induced through a combination of influence from the applied field (cross-activation) and through magnetic interaction between manipulators (cross-talk). The latter may extend to a failure point, defined as the minimum distance D between the two manipulators at which the attraction force between them cannot be overcome by the application of fields or gradients. It is apparent from the manipulator motions (Figure 8) that as separation distance D is reduced, the cross-talk influence increases (even prior reaching the failure point). This is most apparent for actuation scenarios where manipulators bend toward each other, thus temporarily reducing their effective separation distance and increasing cross-talk (**Table 7** and **8**).

Figure 9 and 10 show the results for the independent actuation tests for the left (Figure 9A and 10A) and right (Figure 9B and 10B) manipulators under the OM and PM strategies, respectively, for five different separation distances. For comparison, **Figure 11** shows the combined manipulator characterization results for both presented magnetization strategies. Pose information collected via motion tracking is projected in the X–Y plane, alongside the ideal manipulator trajectory, represented as dashed lines. The data points representing maximum deflection in each direction ($-x$, x, y, $-y$) are connected to represent the approximated reachable area/workspace of each manipulator (**Table 9**).

Manipulators utilizing the PM strategy (Figure 10, and 11B) show the greatest range of motion at the largest separation distance ($D = 4$ cm) and show a reduction in range of motion as the
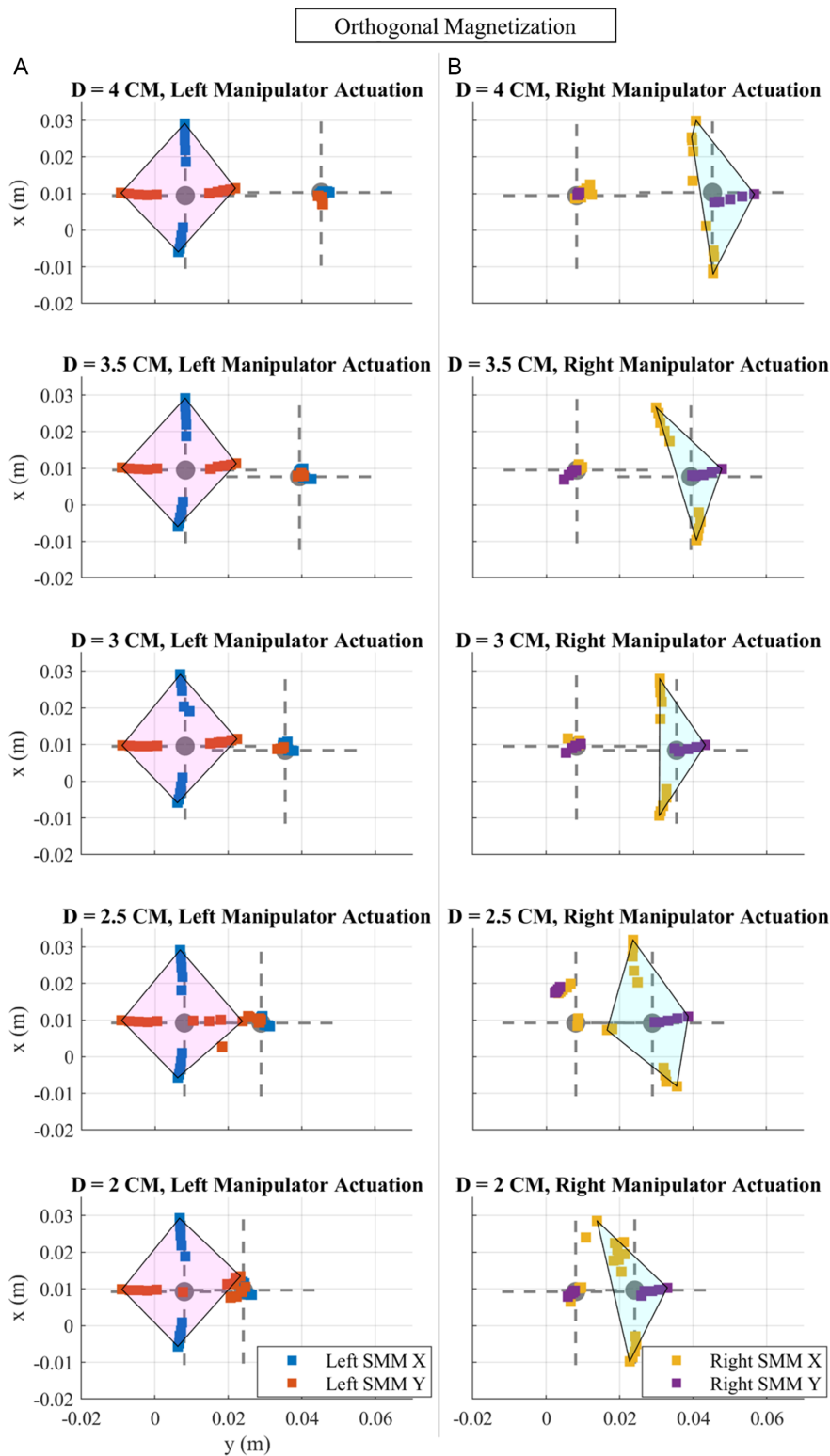
Figure 9. Combined results of independence testing at distance *D* for OM strategy. The colors indicate each segment's motion, and corresponding colors on the opposing manipulator show its motion, while expected to be static. Dashed lines represent ideal linear trajectory. A) Activation of right manipulator. B) Activation of left manipulator. Polygons drawn between maximum bending in each direction represent approximation of the reachable workspace of manipulator.
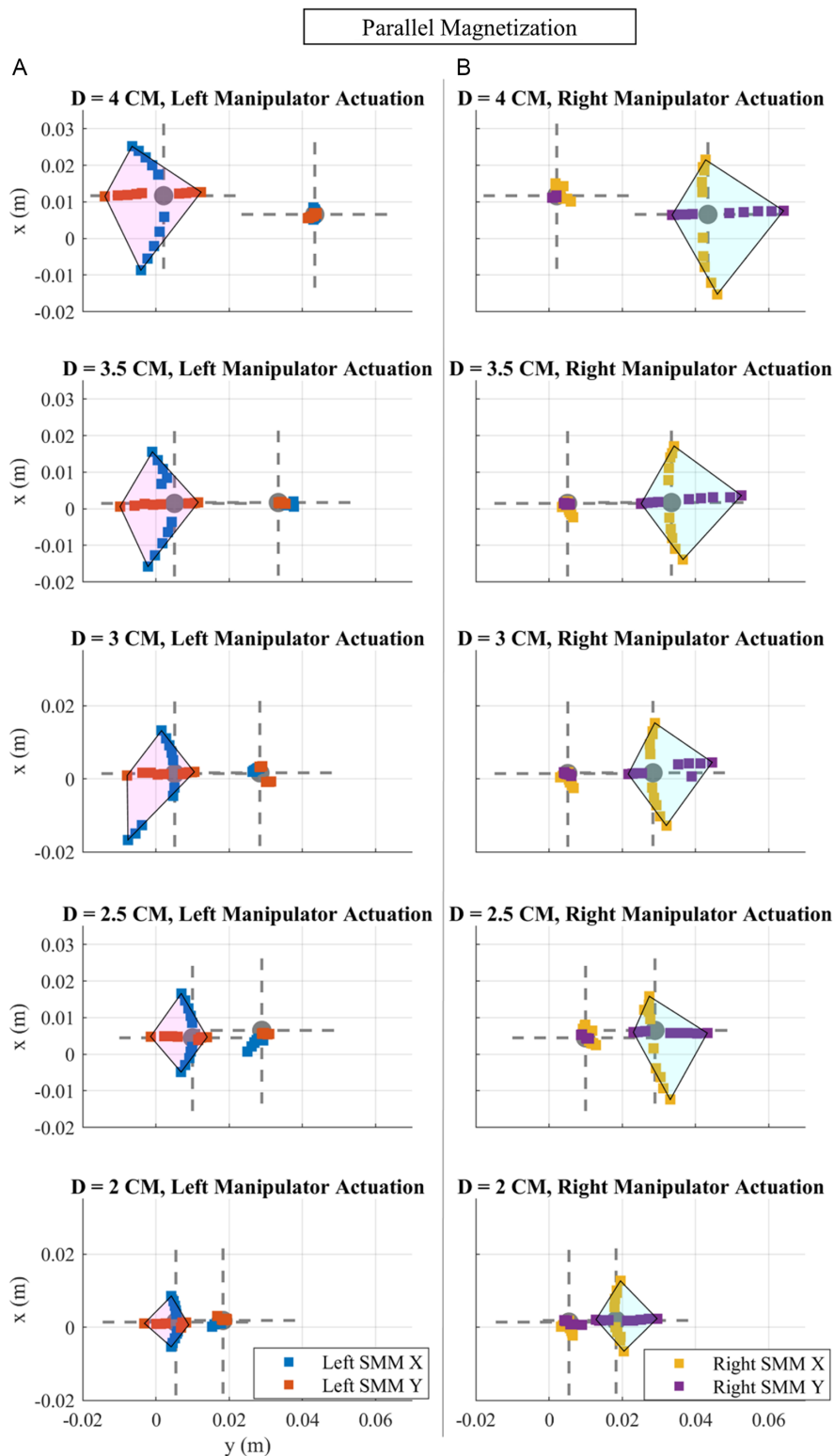
ADVANCED
SCIENCE NEWS
www.advancedsciencenews.com

ADVANCED
INTELLIGENT
SYSTEMS
Open Access
www.advintellsyst.com

Figure 10. Combined results of independence testing at distance *D* for PM strategy. The colors indicate each segment's motion, and corresponding colors on the opposing manipulator show its motion, while expected to be static. Dashed lines represent ideal linear trajectory; A) Activation of right manipulator. B) Activation of left manipulator. Polygons drawn between maximum bending in each direction represent approximation of the reachable workspace of manipulator.

Table 7. Average error of position (mm) from linear trajectory (dashed lines in Figure 9) for orthogonal magnetization strategy.

Orthogonal Magnetization						
Position error of actuated SMM from linear trajectory (mm)						
	Direction of bending	D = 4 cm	D = 3.5 cm	D = 3 cm	D = 2.5 cm	D = 2 cm
Left SMM actuated	+x, −x	0.68	0.76	1.17	1.00	1.03
	+y, −y	0.86	0.77	0.70	1.12	1.1
Right SMM actuated	−x, +x	2.9	5.0	4.00	4.65	3.41
	+y	1.7	0.88	0.70	0.54	0.56

separation distance decreases. This effect is a consequence of the PM strategy. As the proximity of the actuated manipulator with respect to the unactuated manipulator (located at the focal point p) reduces, the field induced at the actuated manipulator will be lower, as expressed by Equation (5). Additionally, we observe an asymmetry in the reachable workspace between left and right manipulator at the same separation distances in the PM strategy (Figure 10 and 11B). This is due to limitations in the calibration accuracy, i.e., if the center of the magnetic workspace is not exactly located in the middle of the two manipulators, the magnitude of the magnetic field applied on the left and right SMMs will not be the same, leading to asymmetrical bending behaviors (Figure 11 and Table 9).

These effects are not present for the OM strategy (Figure 9 and 11A), where the calculated area for actuation of the left manipulator in OM case is similar for all tested distance, and area for the right manipulator fluctuates due to the cross-talk at smaller separation distances.

Specifically, distances $D = 2.5$ cm and $D = 2$ cm (Figure 9), show disturbance in expected motion as well as instability of the nonactuated manipulators, for both left and right manipulator actuation (**Table 10** and **11**). These inaccuracies are caused by attraction between manipulators, which can be observed in the Video S1, Supporting Information. In the same case, inward motion (direction −y) with right manipulator was not possible with application of gradient $-\frac{\partial B_x}{\partial y}$ as expected from Table 5. This field condition caused torsion about main axis, flipping magnetization direction of the manipulator, leading to bending in y direction (outward), which is actuated by application of gradient $\frac{\partial B_x}{\partial y}$.

From analysis of all collected data and videos, it can be seen that in some field conditions, the right SMM in the orthogonally magnetized strategy experiences torsional forces (Video S1, Supporting Information), when expected to be static. This is caused by the unstable condition being realized between the magnetization vector (μ_x) applied field (B_y) in this case, aiming to actuate left SMM (described in Section 2.1).

Due to axial magnetization of both SMMs in the second strategy, no unstable actuation conditions are imposed, hence manipulators do not experience torsional deformation (Table 5 and Video S2, Supporting Information).

Analysis of Figure 9–11 and Videos S1 and S2, Supporting Information, showed that independent control of left and right SMMs was possible at all tested distances for both actuation strategies. Therefore, we can conclude that "the smallest possible distance" for OM and PM strategies is 2 cm.

2.3.4. Phantom Testing

Analysis of characterization results shows pros and cons of the two presented actuation strategies. Suitability of each strategy should be considered depending on the intended application, including requirements range of motion and size of the anatomical cavity. Considering anatomical constraints (**Figure 12**) and the desire to maximize range of motion, priority was given to the increased range of motion at smaller separation distances offered by the OM strategy (Figure 9), over providing bending modalities in four directions.

To produce concept bimanual surgical tools for the endonasal application, two dual-segment manipulators based on the OM strategy (Figure 6) were integrated with functional components. The fabrication technique detailed in Figure 5 was adapted to accommodate a 2 mm camera (0.03 g) (160 k WLC CMOS, Fujikura, Japan) in the left manipulator and an optical fiber (FG105UCA, Thorlabs, USA) in the right manipulator (Figure 14).

Using our large workspace dual-arm robotic magnetic field control system (**Figure 13**), we assessed independent manipulators within an anatomically accurate skull phantom manufactured using real patient computer tomography (CT) scan data (Phacon, Germany) and mechanically realistic materials. Our design requirements for this system were based on currently used EES tools, as well as analysis of anatomical pathways and workspace within the nasal cavities basing on the CT scan data.

The phantom was prepared according to the surgical standards for EES procedures by an ENT surgeon, by partial removal of nasal turbinates, distal septum, and a part of sphenoid bone to widen the workspace for manipulators and for access to access the pituitary socket. A silicone target was placed in the workspace on the wall of sella turcica, the bone of the pituitary fossa as indicated in **Figure 14**.

Manipulators with camera, fiber, and their connections were attached to flexible tubes and fixed on a 3D-printed holder above the phantom. The distal ends of the manipulators were inserted into the nostrils and advanced to position within the target workspace, as seen in Figure 14. Once in place, the left manipulator with embedded camera was first independently actuated to allow inspection of the workspace (Video S3, Supporting Information). Subsequently, the right manipulator with embedded fiber was independently actuated to test its range of motion while the camera (left manipulator) was held still. After evaluating that sufficient range of motion can be provided to reach the target with the light source, the manipulator was actuated to an optimal pose, the light source was turned on and magnetic field was modulated multiple times from 5 to 7 mT in X direction to create repeated linear motion on the target, mimicking a laser beam ablating an adenoma (Video S3, Supporting Information). In the Video S3, Supporting Information, the position of the laser tip was evaluated as a part of post-processing analysis. Each point was determined through identification of the middle (maximum brightness) of the laser tip as the manipulator moves in the view of the external camera. We found the average error to be 0.13 mm
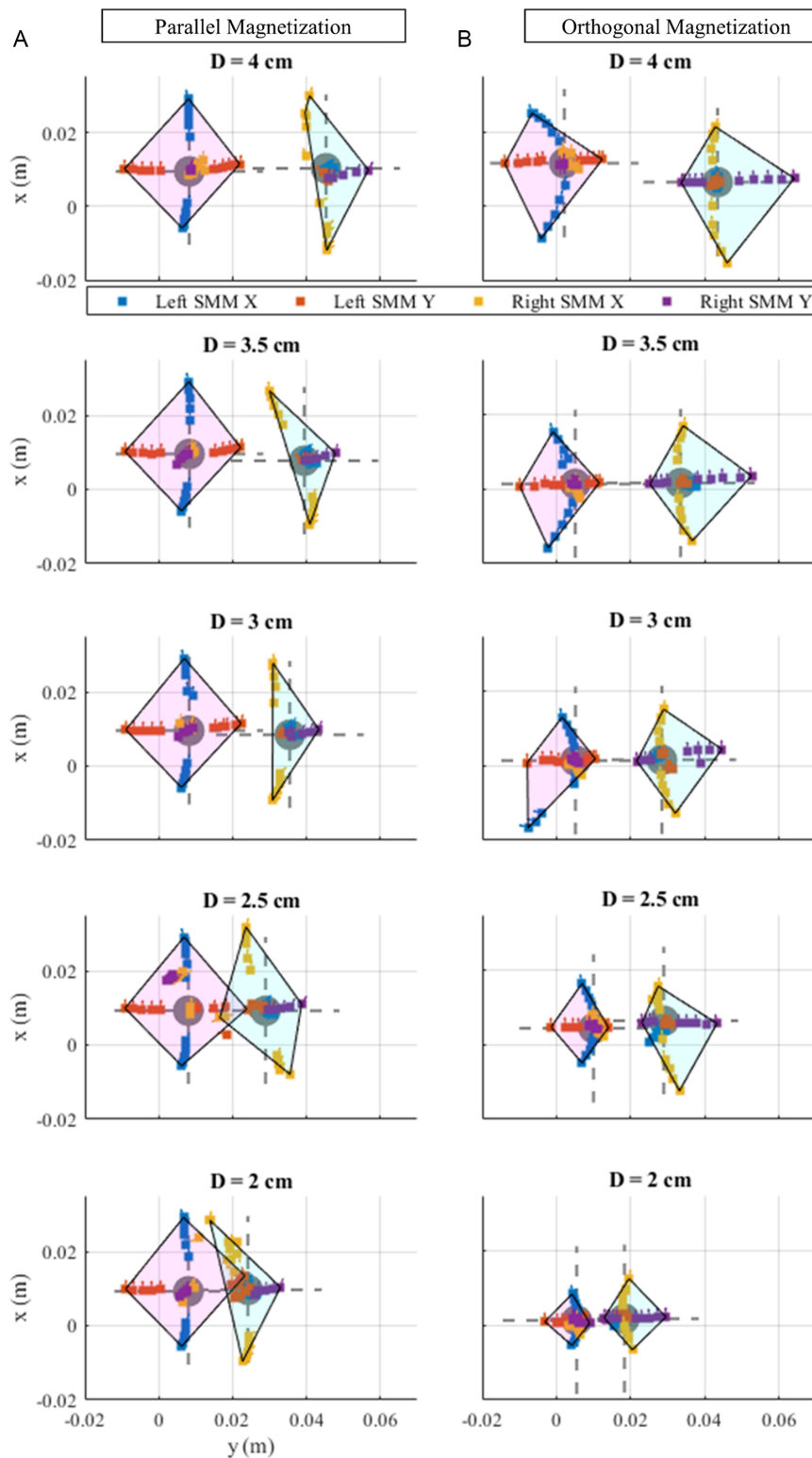
**ADVANCED
SCIENCE NEWS**

www.advancedsciencenews.com

**ADVANCED
INTELLIGENT
SYSTEMS**

www.advintellsyst.com

Figure 11. Combined results of independence testing at distance *D*. The colors indicate each segment's motion, and corresponding colors on the opposing manipulator show its motion, while expected to be static. A) Orthogonal magnetizations strategy. B) Parallel magnetizations strategy. Polygons drawn between maximum bending in each direction represent approximation of the reachable workspace of each manipulator in all evaluated cases.

Table 8. Average error of position (mm) from linear trajectory (dashed lines in Figure 10) for parallel magnetization strategy.

Paralell Magnetization						
Position error of actuated SMM from linear trajectory (mm)						
	Direction of Bending	$D = 4$ cm	$D = 3.5$ cm	$D = 3$ cm	$D = 2.5$ cm	$D = 2$ cm
Left SMM actuated	$+x, -x$	3.95	3.78	4.17	1.33	0.53
	$+y, -y$	0.58	0.58	0.29	0.29	0.40
Right SMM actuated	$-x, +x$	1.33	0.80	0.93	1.79	0.73
	$+y$	0.43	0.77	1.25	0.57	0.18

Table 9. Numerical value of workspace for left and right manipulator approximated based on maximum bendingin tested directions as depicted in Figure 9 and 10.

	Area [cm^2]			
	Orthogonal magnetization		Parallel magnetization	
D (cm)	Left SMM	Right SMM	Left SMM	Right SMM
2	0.56	0.29	0.08	0.16
2.5	0.58	0.46	0.17	0.28
3	0.55	0.23	0.27	0.33
3.5	0.55	0.23	0.33	0.43
4	0.55	0.32	0.45	0.56

Table 10. Error values for position of the static SMMs (cross-activation) for orthogonal magnetization.

Orthogonal Magnetization						
Position error for static SMM [%]						
	Direction of bending	$D = 4$ cm	$D = 3.5$ cm	$D = 3$ cm	$D = 2.5$ cm	$D = 2$ cm
Left SMM actuated	$+x$	5.27	12.77	12.62	8.76	9.66
	$-x$	14.97	1.98	15.22	16.65	17.65
	$+y$	198.5	8.23	6.85	50.3	25.07
	$-y$	7.15	1.98	5.06	18.99	4.09
Right SMM actuated	$+x$	23.75	7.7	9.12	37	72
	$-x$	6.79	9.49	7.03	9.76	9.58
	$+y$	8.4	64.8	54.4	80.65	39.28
	$-y$	50.36	7.73	7.03	76.71	72.24

Table 11. Error values for position of the static SMMs (cross-activation) for parallel magnetization.

Paralell Magnetization						
Position error for static SMM (%)						
	Direction of bending	$D = 4$ cm	$D = 3.5$ cm	$D = 3$ cm	$D = 2.5$ cm	$D = 2$ cm
Left SMM actuated	$+x$	9.26	0.65	16.95	56.11	46.32
	$-x$	9.19	23.23	6.09	26.88	13.24
	$+y$	21.1	29.9	72.17	57	70
	$-y$	4.09	5.337	14.56	8.42	12.39
Right SMM actuated	$+x$	27.61	26.37	30.57	36.58	34.99
	$-x$	27.	26.37	30.57	36.58	34.99
	$+y$	15.28	11.73	15.28	18.77	29.19
	$-y$	69	5.5	6.8	10.13	12.31

manipulators and attraction occurred only with higher field magnitude of 7 mT. In this case, application of $-By$ caused reciprocal attraction and the opposite field (By) was applied to induce their separation (Video S4, Supporting Information).

3. Discussion and Conclusions

In this article, we present for the first time a dual-magnetic manipulator system for medical applications in confined workspaces. We developed a geometrically optimized design of a SMM to provide preferential bending planes and high angles of deflection. When configured into two parallel manipulators (Figure 6 and 7), independent magnetic manipulation is possible via two distinct actuation strategies. These utilize specific manipulator magnetization profiles (OM strategy) and local magnetic field gradient control (PM strategy), respectively, and are implemented using our dEPM robotic platform.

Characterizing the two strategies as a function of manipulator separation, assessing the range of motion and the effect of manipulator interacting forces during independent manipulator actuation, identified associated advantages and disadvantages for each. The presented PM strategy (Figure 10) shows consistent biplanar actuation with minimal manipulator cross-talk for all separation distances. However, this strategy suffers from a reduction in bending range of motion (and thus workspace) for smaller separations due to weaker induced magnetic fields on the actuated manipulator. It is also notable that achieving independent actuation via this method is highly coupled to the calibration accuracy of the dEPM system and identification and alignment of the focal point, with even a small movement in the focal point causing both agents to be simultaneously actuated. Additionally, the calibration accuracy can also affect the symmetry in the reachable workspace of the left and right manipulator. To resolve these accuracy issues, the calibration methods for the dEPM platform can be improved through implementing more accurate optical tracking system in the future. This issue is far less significant for the presented OM strategy (Figure 9), where actuation is induced primarily via homogeneous magnetic fields, relaxing the accuracy requirements of the dEPM system.
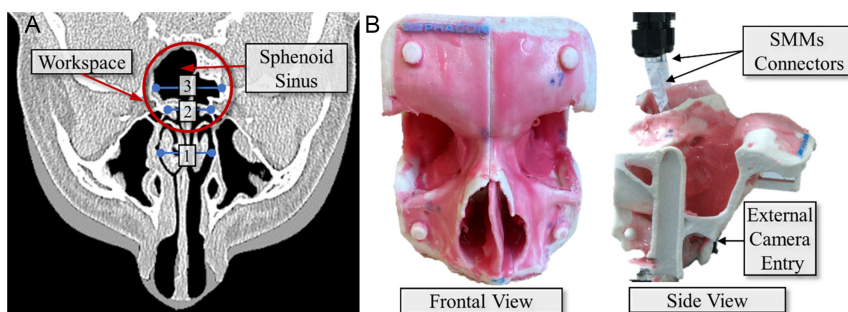
with standard deviation of 9.8% and the highest positional error of 0.34 mm. In this experiment, the manipulators were positioned at the distance D between 22.8 to 31.4 mm (based on the CT scan (**Table 12**)). Considering results for OM testing (Figure 9 and Video S1, Supporting Information), attraction in case of inward bending was expected with lowest magnitude conditions (3 mT). However, the anatomical features of the workspace provided increased mechanical separation of the

Figure 12. A) A horizontal slice of a CT scan from patient "Meyer" used to manufacture skull phantom used in this study (source: phacon.de) with highlighted workspace of interest. B) Photographs of the phantom including frontal and side view with highlighted entry for an external camera with light source.
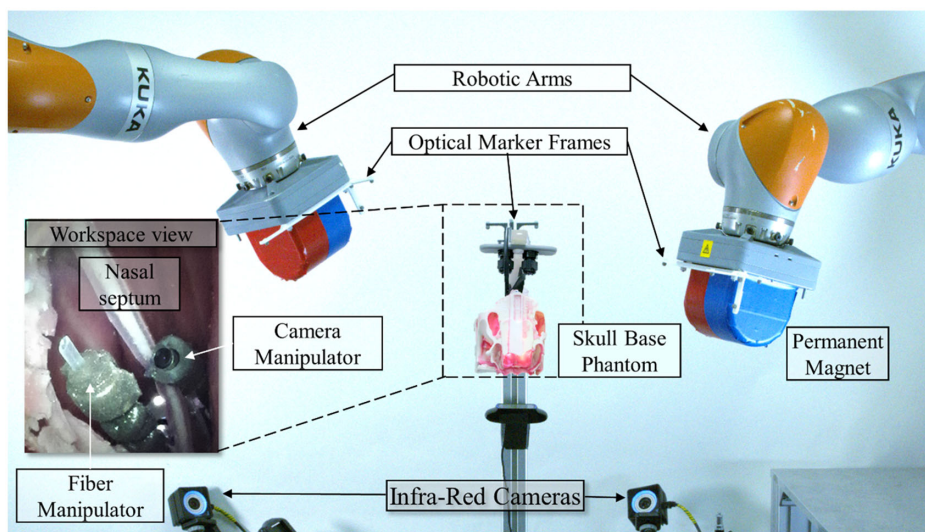

Figure 13. Experimental set up for phantom testing, with a close-up view of a workspace accessed with a camera and a light source through an opening in the sella bone.
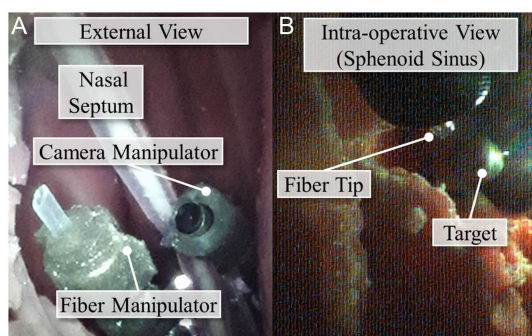

Figure 14. A) View from the endoscopic camera attached in the phantom for bottom view of the site. B) Intra-operative view from the camera embedded into one of the manipulators.

Using the OM strategy, the nonactuated manipulator will ideally remain stationary until a certain unique magnetic field is applied. However, as evidenced through the presented OM independent actuation tests (Figure 9 and 11A), separation distance influences the level of independent motion achievable due to the effects of

Table 12. Approximated workspace size in the skull base phantom based on the CT scan.

	Distal nostrils width (1)	Distal nasal cavity, opening to the sphenoid sinus (2)	Workspace width (sphenoid sinus) (3)
Size (mm)	24.7	22.8	31.4

magnetic interaction (cross-talk) between the manipulators. Furthermore, under the application of gradient $-\frac{\partial B_x}{\partial y}$ to the right manipulator, the desired inward motion (direction $-y$) is not achieved. This is due to the induced magnetic field's orientation with respect to the manipulator's magnetization causing torsion about its main axis, effectively flipping the magnetization direction of the manipulator and leading to undesired bending in $+y$ direction (outwards) instead (Video S1, Supporting Information).

Independent control was possible at all tested distances, with different levels of cross-talk and cross-activation, depending on the actuation strategy and separation distance, where the smallest

tested separation distance was 2 cm. The smallest possible distance (function of cross-talk) will vary with change in manipulator length, diameter, elastomeric properties, and amount of magnetic material. Therefore, depending on the exact application of the dual-manipulator system, SMM's dimensions will vary and with those—the amount of cross talk and smallest distance at which SMMs can still achieve independent control.

Regardless of the identified limitations of the proposed strategies, independent motion of the two parallel manipulators was possible over a large area for both (up to 0.55 and 0.32 cm^2 for OM strategy and up to 0.45 and 0.56 cm^2 for PM strategy). Although the achievable range of motion would increase with the removal of the marker frames (required for tracking), successful actuation with this payload indicates potential suitability for surgical tool manipulation with confined anatomy. This proposed system was thus evaluated for the scenario of EES (Figure 13 and 14) and independent actuation of two manipulators (with camera and optical fiber, respectively). This was qualitatively tested in the confined endonasal space of a 3D-printed base skull phantom. Evaluation of laser tip position showed the average positional error of 0.13 mm. Further feasibility tests in terms of clinical application should be performed in future works. Evaluation of maximum payload possible to manipulate at the tip is of interest for surgical applications requiring tool–tissue interaction such as the use of cutting tools, ultrasound probes, or forceps. Moreover, the quantification and optimization of speed of tasks performed with the presented bimanual manipulator system will be of interest for any practical application to surgical scenarios.

Future adaptions may leverage the discrete modular approach proposed to deliver different configurations of multiple short segments for increased maneuverability and/or range of motion, or to facilitate controlled navigation approaches. To enhance the stability of the system when the OM strategy is applied, approaches to increase torsional stiffness of one of both manipulators may be explored ([16,36]). Additionally, integration of proprioceptive and localization feedback would aid navigating in visually obscured clinical scenarios (based on preoperative anatomical scans) and allow for stable focal point tracking and independent closed loop manipulator control.

The proposed design approach and actuation strategies demonstrate independent actuation of two magnetic continuum manipulators within the same confined workspace. This opens a new approach to magnetically controlled surgical tools suited to application within confined, delicate anatomy. Coupling the scalability of monolithic magnetic manipulators with independent local actuation offers prospects for improving endoscopic procedures currently served by large and rigid tools, with associated benefit to the patient and surgeon.

Supporting Information

Supporting Information is available from the Wiley Online Library or from the author.

Acknowledgements

Conflict of Interest

The authors declare no conflict of interest.

Data Availability Statement

The data that support the findings of this study are available from the corresponding author upon reasonable request.

Keywords

[1] P. E. Dupont, B. J. Nelson, M. Goldfarb, B. Hannaford, A. Menciassi, M. K. O'Malley, N. Simaan, P. Valdastri, G. Yang, *Sci. Robot.* **2021**, *6*, 1.

[2] T. da Veiga, J. H. Chandler, P. Lloyd, G. Pittiglio, N. J. Wilkinson, A. K. Hoshiar, R. A. Harris, P. Valdastri, *Progr. Biomed. Eng.* **2020**, *2*, 032003.

[3] A. Bajo, N. Simaan, *Int. J. Rob. Res.* **2016**, *35*, 422.

[4] H. B. Gilbert, D. C. Rucker, R. J. Webster, *Springer Tracts Adv. Robot.* **2016**, *114*, 253.

[5] R. Wirz, L. G. Torres, P. J. Swaney, H. Gilbert, R. Alterovitz, R. J. Webster III, K. D. Weaver, P. T. Russell III, *Neurosurgery* **2015**, *76*, 479.

[6] N. Simaan, K. Xu, W. Wei, A. Kapoor, P. Kazanzides, R. Taylor, P. Flint, *Int. J. Rob. Res.* **2009**, *28*, 1134.

[7] M. Runciman, A. Darzi, G. P. Mylonas, *Soft Robot.* **2019**, *6*, 423.

[8] M. McCandless, A. Perry, N. DiFilippo, A. Carroll, E. Billatos, S. Russo, *Soft Robot.* **2021**, *1*, 1.

[9] M. Brancadoro, M. Manti, F. Grani, S. Tognarelli, A. Menciassi, M. Cianchetti, *Front. Robot. AI* **2019**, *6*, 1.

[10] F. Campisano, A. A. Remirez, C. A. Landewee, S. Calo, K. L. Obstein, R. J. Webster, P. Valdastri, *IEEE Robot. Autom. Lett.* **2020**, *5*, 6427.

[11] T. Da Veiga, J. H. Chandler, G. Pittiglio, P. Lloyd, M. Holdar, O. Onaizah, A. Alazmani, P. Valdastri, *IEEE 4th Inter. Conf. on Soft Robotics (RoboSoft)*, IEEE, Piscataway, NJ **2021**.

[12] G. Z. Lum, Z. Ye, X. Dong, H. Marvi, O. Erin, W. Hu, M. Sitti, *Proc. Natl. Acad. Sci. USA* **2016**, *113*, E6007.

[13] Y. Kim, E. Genevriere, P. Harker, J. Choe, M. Balicki, A. B. Patel, X. Zhao, *Proc. IEEE Int. Conf. Robot. Autom.*, **2022**, 9600.

[14] Y. Kim, E. Genevriere, P. Harker, J. Choe, M. Balicki, R. W. Regenhardt, J. E. Vranic, A. A. Dmytriw, A. B. Patel, X. Zhao, *Sci. Robot.*, **2022**, *7*, 1.

[15] G. Pittiglio, P. Lloyd, T. da Veiga, O. Onaizah, C. Pompili, J. H. Chandler, P. Valdastri, *Soft Robot.* **2022**, *1*, 1.

[16] P. Lloyd, O. Onaizah, G. Pittiglio, D. K. Vithanage, S. Member, J. H. Chandler, P. Valdastri, *IEEE Robot. Autom. Lett.* **2022**, *7*, 9770.

[17] T. Wang, H. Ugurlu, Y. Yan, M. Li, M. Li, A. Wild, E. Yildiz, M. Schneider, D. Sheehan, W. Hu, M. Sitti, *Nat. Commun.* **2022**, *13*, 1.

[18] M. Richter, M. Kaya, J. Sikorski, L. Abelmann, V. K. Venkiteswaran, S. Misra, *Soft Robot.* **2023**, *10*, 3.

[19] C. M. Heunis, Y. P. Wotte, J. Sikorski, G. P. Furtado, S. Misra, *IEEE Robot. Autom. Lett.* **2020**, *5*, 704.

[20] S. Tottori, L. Zhang, K. E. Peyer, B. J. Nelson, *Nano Lett.* **2013**, *13*, 4263.

[21] E. Diller, J. Giltinan, M. Sitti, *Int. J. Rob. Res.* **2013**, *32*, 614.

[22] I. S. M. Khalil, A. F. Tabak, Y. Hamed, M. Tawakol, A. Klingner, N. El Gohary, B. Mizaikoff, M. Sitti, *IEEE Robot. Autom. Lett.* **2018**, *3*, 1703.

[23] J. Giltinan, P. Katsamba, W. Wang, E. Lauga, M. Sitti, *Appl. Phys. Lett.* **2020**, *116*, 134101-1.

[24] P. Katsamba, E. Lauga, *Phys. Rev. Appl.* **2016**, *5*, 1.

[25] E. Diller, S. Floyd, C. Pawashe, M. Sitti, *Proc. IEEE Int. Conf. Robot. Autom.*, **2011**, *28*, 115.

[26] S. Miyashita, E. Diller, M. Sitti, *Int. J. Robot. Res.* **2013**, *32*, 591.

[27] M. Salehizadeh, E. Diller, *J. Micro-Bio Robot.* **2017**, *12*, 9.

[28] M. Salehizadeh, E. Diller, in *2017 Int. Conf. on Manipulation, Automation and Robotics at Small Scales (MARSS)*, IEEE **2017**.

[29] J. Rahmer, C. Stehning, B. Gleich, *Sci. Robot.* **2017**, *2*, 1.

[30] F. Ongaro, S. Pane, S. Scheggi, S. Misra, *IEEE Trans. Robot.* **2019**, *35*, 174.

[31] E. Diller, J. Giltinan, G. Z. Lum, Z. Ye, M. Sitti, *Int. J. Robot. Res.* **2016**, *35*, 114.

[32] S. Salmanipour, E. Diller, *Proc. IEEE Int. Conf. Robot. Autom.* **2018**, 3608.

[33] G. Pittiglio, M. Brockdorff, T. da Veiga, J. Davy, J. H. Chandler, P. Valdastri, *IEEE Trans. Robot.* **2022**, *1*, 1.

[34] T. Terada, K. Kovacs, L. Stefaneanu, E. Horvath, *Endocr. Pathol.* **1995**, *6*, 301.

[35] E. R. Constantino, R. Leal, C. C. Ferreira, M. A. Acioly, J. A. Landeiro, *Arq. Neuropsiquiatr.* **2016**, *74*, 388.

[36] P. Lloyd, Z. Koszowska, O. Onaizah, J. H. Chandler, P. Valdastri, *Front. Robot. AI* **2021**, *8*, https://doi.org/10.3389/frobt.2021.715662.